Research Article Vol. 56, No. 23 / August 10 2017 / Applied Optics 6639

applied optics

Analysis of a holographic laser adaptive optics system using a deformable mirror

Kainan Yao, Jianli Wang,* Xinyue Liu, Xudong Lin, and Lu Chen

Changchun Institute of Optics, Fine Mechanics and Physics, Chinese Academy of Sciences, Changchun, Jilin 130033, China
**Corresponding author: wangjianli@ciomp.ac.cn*

Received 4 May 2017; revised 13 July 2017; accepted 14 July 2017; posted 17 July 2017 (Doc. ID 295217); published 10 August 2017

We describe a closed-loop holographic laser adaptive optics system (HLAOS) based on a holographic wavefront sensor (HWFS) and 21-element continuous-surface piezoelectric deformable mirror (DM). The principle behind HWFSs is described, and then the response sensitivity and crosstalk effect on the lowest 12 Zernike modes of aberration are analyzed. Next, the wavefront-correction capability of the 21-element DM is analyzed. The closed-loop correction of the HLAOS to a static aberration is then numerically simulated. We report a practical implementation of the HLAOS and compare the aberration-compensation effect with a traditional adaptive optics system based on a 37-unit Shark–Hartmann sensor. The practically relevant parameters are analyzed and the experimental results show that an HLAOS using a piezoelectric DM can achieve a correction capability comparable to that of a traditional adaptive optics system.

OCIS codes: (010.1080) Active or adaptive optics; (010.1285) Atmospheric correction; (010.7350) Wave-front sensing; (090.1760) Computer holography.

https://doi.org/10.1364/AO.56.006639

1. INTRODUCTION

Adaptive optics has a wide range of laser technology applications, such as in inertial confinement fusion laser systems, free-space optical communication systems, and laser weapon systems [1]. The wavefront sensor, which measures the real-time wavefront aberration as a feedback element, is an important part of an adaptive optics system [2].

In 2000, a modal wavefront sensor was first proposed by Neil and Booth [3,4], and the possible application of holographic elements in modal wavefront sensors was suggested. Compared with a Shack–Hartmann wavefront sensor, a holographic wavefront sensor (HWFS) requires fewer calculations for wavefront sensing [5]. Several studies have applied computer-generated holographic elements to a modal wavefront sensor and corrected the response curve, where the detection accuracy of a single Zernike-mode aberration can reach $\lambda/50$ [6–14]. Changhai *et al.* used a plane wave in combination with a Fourier lens to replace spherical waves, improving the energy-utilization efficiency [15–17]. An HWFS was first used in an ocular wavefront aberration-detection system by Corbett *et al.* [18]. A method to optimize the response curve was proposed by Dong *et al.*, and a low-resolution Shack–Hartmann sensor combined with a holographic-mode wavefront sensor was suggested to expand the dynamic range of wavefront detection [19,20].

We previously reported a closed-loop dynamic holographic adaptive optics system [21] and discussed the application of an HWFS in free-space optics communications [22].

In this study, a holographic laser adaptive optics system (HLAOS) was established using an HWFS and a 21-element continuous-surface piezoelectric deformable mirror (DM). Then, the closed-loop aberration-compensation process was numerically simulated. An experimental setup was also established and compared to the results obtained with the aberration-compensation effect of a traditional adaptive optics system based on a 37-unit Shark–Hartmann wavefront sensor.

2. THEORETICAL ANALYSIS FOR HWFS

The basic principle of the HWFS is shown in Fig. 1. Sub-hologram 1 is produced through the interference of the Zernike-mode $bZ_i(x,y)$ aberration light-wave $O_1(x,y)$ and a reference spherical wave $R_1(x,y)$ converging at point A (x_A, y_A, z_A). Sub-hologram 2 is produced through the interference of the same Zernike-mode $-bZ_i(x,y)$ aberration light-wave $O_2(x,y)$ and a reference spherical wave $R_2(x,y)$ converging at point B (x_B, y_B, z_B). By virtue of the properties of multiplexing holographic elements, the two sub-holograms are superimposed to form a multiplexed hologram that contains the Zernike-mode aberration information.

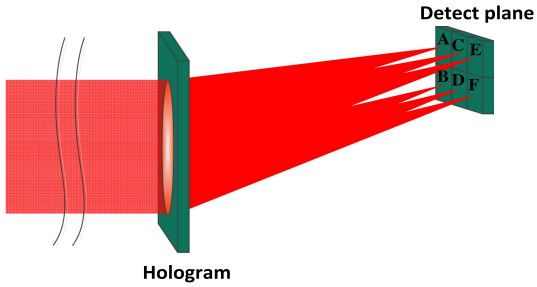

Fig. 1. Schematic of HWFS.

First, two holograms were defined, the light transmittance functions of which are

$$\begin{aligned} h_{2i-1}(x,y) &= |O_{2i-1}(x,y) + R_{2i-1}(x,y)|^2 \\ &= O_{2i-1}(x,y)^2 + R_{2i-1}(x,y)^2 \\ &\quad + O_{2i-1}(x,y)R^*_{2i-1}(x,y) + O^*_{2i-1}(x,y)R_{2i-1}(x,y) \\ h_{2i}(x,y) &= |O_{2i}(x,y) + R_{2i}(x,y)|^2 \\ &= O_{2i}(x,y)^2 + R_{2i}(x,y)^2 \\ &\quad + O_{2i}(x,y)R^*_{2i}(x,y) + O^*_{2i}(x,y)R_{2i}(x,y). \end{aligned} \tag{1}$$

When using a computer-generated hologram (CGH) instead of an analog hologram recording, we can omit the zero-order terms in Eq. (1) to increase the diffraction efficiency. Thus,

$$\begin{aligned} H_{2i-1}(x,y) &= O^*_{2i-1}(x,y)R_{2i-1}(x,y) \\ &= \exp\{-jbZ_i(x,y)\} \times \exp\{-jk[(x-x_A)^2 \\ &\quad +(y-y_A)^2 + z_A^2]^{1/2}\}, \\ H_{2i}(x,y) &= O^*_{2i}(x,y)R_{2i}(x,y) \\ &= \exp\{jbZ_i(x,y)\} \times \exp\{-jk[(x-x_B)^2 \\ &\quad +(y-y_B)^2 + z_B^2]^{1/2}\}. \end{aligned} \tag{2}$$

When light wave $W(x,y)$ has the same mode of aberration with amplitude a, two spherical waves modulated by an aberration in this mode will emerge and converge at points A and B, respectively:

$$\begin{aligned} H_1(x,y) \times W(x,y) &= \exp\{jaZ_i(x,y)\} \times \exp\{-jbZ_i(x,y)\} \\ &\quad \times \exp\{-jk[(x-x_A)^2 + (y-y_A)^2 \\ &\quad +(z-z_A)^2]^{1/2}\}, \\ H_2(x,y) \times W(x,y) &= \exp\{jaZ_i(x,y)\} \times \exp\{jbZ_i(x,y)\} \\ &\quad \times \exp\{-jk[(x-x_B)^2 + (y-y_B)^2 \\ &\quad +(z-z_B)^2]^{1/2}\}. \end{aligned} \tag{3}$$

According to the HWFS principle, as $a_i = b$, the peak energy at point B is the weakest. As $a_i = -b$, the peak energy at point A is the weakest. Thus, the aberration amplitude of the incident light wave a_i can be obtained by detecting the relative light intensities at points A and B. The relative light intensities at points A and B can be written, in the form of the first moment, as

$$P_W = \frac{I_A - I_B}{I_A + I_B}. \tag{4}$$

To measure more Zernike-mode aberrations according to the characteristics of the holographic element, additional pairs of sub-holograms are superimposed correspondingly and the wave-vector directions of the relevant spherical waves are controlled to spatially separate the focused spots. The corresponding Zernike-mode amplitude can be obtained by measuring the relative light intensity of each pair of spots, and the distorted wavefront can be fitted.

3. NUMERICAL SIMULATION OF THE HWFS

We performed numerical simulations of the HWFS. The simulation parameters were selected as follows: the sampling point of the hologram was 512 × 512, the laser wavelength was 632.8 nm, the aperture of the hologram was 6 mm, the distance between the image and hologram planes was 3000 mm, the distance between the focal spot and axis was more than 10 mm, and the lowest 12 Zernike-mode aberrations were detected to be $Z(2,0)$, $Z(2,-2)$, $Z(2,2)$, $Z(3,-1)$, $Z(3,1)$, $Z(4,0)$, $Z(3,-3)$, $Z(3,3)$, $Z(4,2)$, $Z(4,-2)$, $Z(4,4)$, and $Z(4,-4)$. In this paper, we use the definition of the Zernike polynomials as previously detailed [3]. All Zernike-mode aberration biases were $\pm 0.5\lambda$ (RMS), and 24 sub-holograms were multiplexed in total. This multiplexing was performed by adding up all the sub-holograms. The CGH is encoded as a binary-phase hologram, as shown in Fig. 2.

The optical field distribution on the holographic image plane is shown in Fig. 3(b), assuming the hologram was irradiated by an ideal plane wave. There are 12 pairs of spots on the holographic image plane, and each pair of spots is observed to carry the information of each aberration loaded by the hologram. When the plane wave is incident, the light intensity of each pair of spots is equal. The optical field distribution on the holographic image plane is shown in Figs. 3(a) and 3(c), when the aberration of the incident light wave is $\pm 0.5\lambda$ (RMS) Z(2, 0).

Twenty-four detection apertures of 0.5 mm × 0.5 mm were selected at the center of each spot on the holographic image plane, and the spot energies within the apertures were integrated to calculate the relative light intensity. The response sensitivity of the aberration could be obtained using the incident wave with a particular aberration to irradiate the hologram and change the amplitude of that aberration constantly.

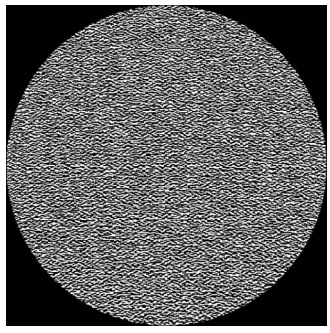

Fig. 2. Computer-generated hologram.

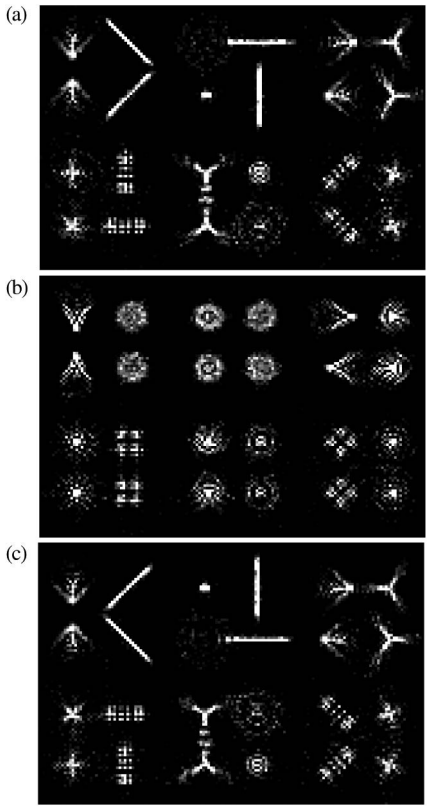

Fig. 3. Spots on the holographic image plane: (a) $+0.5\lambda$ $Z(2, 0)$, (b) without aberration, (c) -0.5λ $Z(2, 0)$.

The response-sensitivity curves of $Z(2, 2)$ and $Z(3, 1)$ are shown in Figs. 4(a) and 4(b).

As shown in Fig. 4, the response-sensitivity curve has good linearity in the case of a small aberration. When the aberration coefficient is zero, the slope of the curve is defined as the response sensitivity of this mode of aberration. As shown in Fig. 4, this approximation is obviously inaccurate in the case of larger aberrations. The approximation accuracy decreases substantially as the aberration increases, however, which does not affect the final closed-loop correction effect in an adaptive optics system because we can accurately detect the "trend" of all mode aberrations. This was verified in a later experiment. Instead, we can draw the conclusion that an HWFS has a higher precision when dealing with small aberration approximations, and the smaller the aberration, the higher the precision.

As also shown in Fig. 4(a), if an incident wavefront only has an aberration of $Z(2, 2)$, the sensor responds not only to the aberration in this mode but also to an aberration of $Z(4, -2)$ to some extent, which is the so-called intermodal crosstalk. To reduce this phenomenon, an initial calibration was performed in the experiment to obtain the response sensitivity matrix S, as shown in Fig. 5, and the zero point O, as shown in Fig. 6. Using this information, every Zernike-mode aberration with wavefront distorted incident light-waves was detected, enabling fitting of the distorted wavefronts.

Aberration Z of various modes can be solved through the first moment P of the output signal of the sensor, as follows:

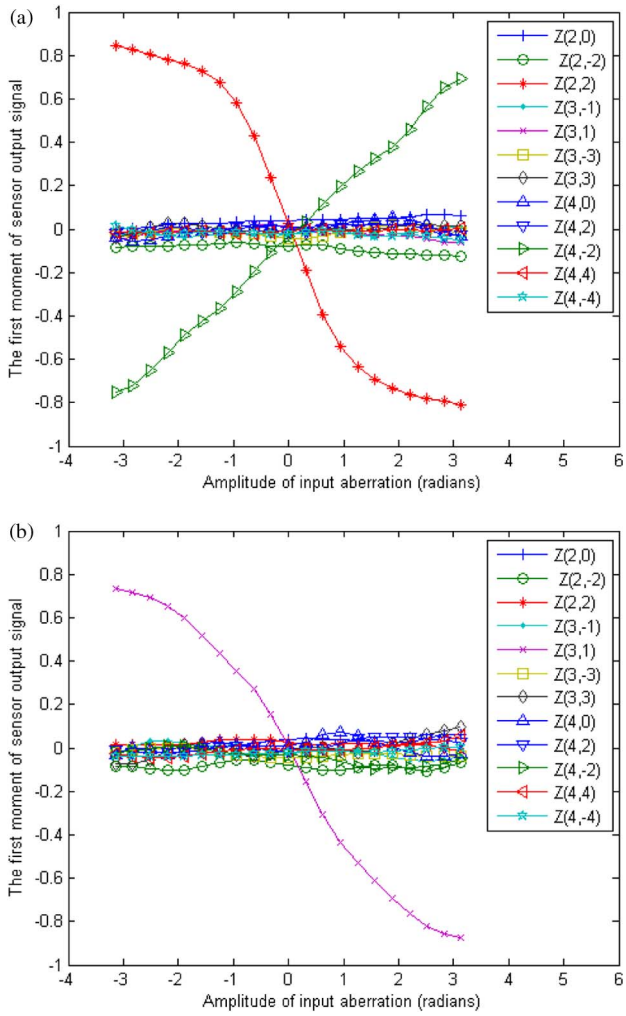

Fig. 4. Sensitivity response curve of (a) $Z(2, 2)$ and (b) $Z(3, 1)$.

$$Z = S^{-1} \times (P - O). \tag{5}$$

If the intermodal crosstalk effect is ignored, all off-diagonal elements of matrix S become 0, which will reduce the wavefront-fitting precision.

The distorted wavefront of the incident light-wave 0.25λ (RMS) is simulated as shown in Fig. 7(a), where the only aberration mode is $Z(2, -2)$. The Zernike coefficients were solved using the relative light intensity data of the holographic image plane spots. The measured wavefront is shown in Fig. 7(b) and the wavefront detection error is 0.134λ (RMS), as shown in Fig. 7(c), when the sensitivity matrix S is a diagonal matrix. For the case when the intermodal crosstalk effect is not ignored, the measured wavefront is shown in Fig. 7(d) and the detection error of 0.068λ (RMS) is shown in Fig. 7(e).

We can draw the following conclusions based on the preceding numerical simulation test: by detecting the relative light intensity of the holographic image plane spots, and by virtue of the pre-calibrated response sensitivity, an HWFS can obtain the coefficients of every Zernike-mode aberration directly. Compared to a Shack–Hartmann wavefront sensor, this sensor has no spot centroid extraction, so it can achieve more rapid

		Input aberration mode											
		Z(2, 0)	Z(2, -2)	Z(2, 2)	Z(3, -1)	Z(3, 1)	Z(3, -3)	Z(3, 3)	Z(4, 0)	Z(4, 2)	Z(4, -2)	Z(4, 4)	Z(4, -4)
The first moment of sensor output	$P_{Z(2,0)}$	1.56	0.08	0.05	0.00	-0.01	0.00	-0.01	-0.21	-0.36	0.00	0.00	0.02
	$P_{Z(2,-2)}$	-0.02	1.55	-0.02	0.03	0.00	-0.03	0.04	0.05	-0.87	-0.08	-0.10	-0.01
	$P_{Z(2,2)}$	-0.01	0.04	1.63	-0.03	-0.01	0.00	-0.03	-0.01	-0.03	-0.85	0.00	0.03
	$P_{Z(3,-1)}$	-0.04	0.02	-0.01	1.24	0.03	0.00	-0.12	0.00	0.04	-0.03	0.01	0.00
	$P_{Z(3,1)}$	-0.04	-0.01	-0.01	0.01	1.23	0.02	-0.03	-0.05	-0.03	-0.02	-0.04	-0.01
	$P_{Z(3,-3)}$	-0.01	-0.01	-0.02	-0.06	0.41	0.95	0.00	0.12	0.10	0.02	-0.01	-0.02
	$P_{Z(3,3)}$	0.01	-0.02	0.02	-0.42	0.02	0.02	0.95	-0.01	-0.03	0.01	0.02	0.01
	$P_{Z(4,0)}$	-0.23	-0.06	-0.01	-0.02	0.01	0.07	-0.01	1.22	-0.24	-0.03	-0.02	0.03
	$P_{Z(4,2)}$	-0.04	-0.33	-0.01	-0.01	-0.08	-0.05	-0.02	0.03	1.77	-0.06	-0.08	0.01
	$P_{Z(4,-2)}$	0.07	-0.01	-0.55	0.00	0.00	-0.02	-0.01	0.02	-0.04	1.65	-0.02	-0.01
	$P_{Z(4,4)}$	0.21	0.04	-0.05	0.04	-0.02	0.01	0.04	0.04	-0.12	-0.05	0.69	-0.01
	$P_{Z(4,-4)}$	0.01	0.03	0.00	0.01	0.03	-0.01	0.02	0.07	-0.09	0.00	0.01	0.67

Fig. 5. Sensitivity matrix S.

	The first moment of sensor output										
	$P_{Z(2,0)}$	$P_{Z(2,-2)}$	$P_{Z(2,2)}$	$P_{Z(3,-1)}$	$P_{Z(3,1)}$	$P_{Z(3,-3)}$	$P_{Z(3,3)}$	$P_{Z(4,0)}$	$P_{Z(4,2)}$	$P_{Z(4,-2)}$	$P_{Z(4,4)}$	$P_{Z(4,-4)}$
Plane wave input	-0.014	0.048	-0.009	-0.042	0.062	-0.037	-0.006	0.033	-0.031	-0.012	0.007	0.026

Fig. 6. Zero point O.

wavefront detection; and with the reduction in aberrations, the detection accuracy increases gradually. This characteristic is suitable for a closed-loop correction system because we can minimize the wavefront distortion through closed-loop corrections.

4. ANALYSIS OF WAVEFRONT-FITTING ABILITY OF 21-ELEMENT CONTINUOUS-SURFACE DM

A numerical model was built for a self-made 21-element continuous-surface DM; the specific parameters of this type of DM were described in detail previously [23]. The aperture of the simulated 21-element continuous-surface DM was 50 mm, the piezoelectric actuators adopted a 5×5 square array, and four diagonal actuators were removed. The spacing of two adjacent actuators was 9 mm, and the response function crosstalk was 20%. In the following analyses, assuming all actuators have a consistent response function, they were assigned a Gaussian function approximation uniformly, whereas in practical applications, the response function of each actuator could be measured directly. The response function of the center actuator is shown in Fig. 8(a), and Fig. 8(b) shows the waffle mode of the 21-element continuous-surface DM.

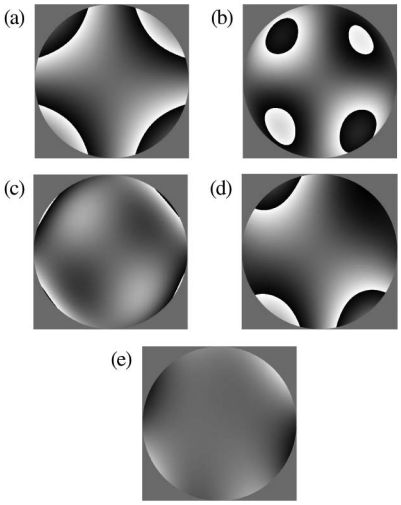

Fig. 7. (a) Distorted wavefront, (b) detected wavefront when the intermodal crosstalk effect is ignored, (c) wavefront-detection error when the intermodal crosstalk effect is ignored, (d) detected wavefront when intermodal crosstalk is reduced, and (e) wavefront detection error when intermodal crosstalk is reduced.

In the following experiment, the least squares method was used to analyze the ability of the 21-element continuous-surface DM to fit the lowest 16 Zernike-mode aberrations. Figures 8(c)–8(f) show the ideal wavefronts of the $Z(2, 0)$, $Z(2, -2)$, $Z(3, -1)$, and $Z(5, -1)$ Zernike-mode aberrations, respectively. Figures 8(g)–8(j) show the fitting results. As shown in Fig. 8, the 21-element continuous-surface DM is able to fit the $Z(2, 0)$, $Z(2, -2)$, and $Z(3, -1)$ aberrations well, while its fit for the $Z(5, -1)$ aberration is poor.

To quantitatively evaluate the ability of the 21-element continuous-surface DM to fit each Zernike-mode aberration, we defined the fitting error as the RMS value ratio of the residual wavefront to the ideal Zernike-mode wavefront aberration.

Figure 9 shows the fitting errors of the lowest 16 Zernike-mode aberrations, i.e., the fitting errors of $Z(2, 0)$, $Z(2, -2)$, $Z(2, 2)$, $Z(3, -1)$, $Z(3, 1)$, $Z(4, 0)$, $Z(3, -3)$, $Z(3, 3)$, $Z(4, 2)$, $Z(4, -2)$, $Z(4, 4)$, $Z(4, -4)$, $Z(5, 1)$, $Z(5, -1)$, $Z(5, 3)$, and $Z(5, -3)$. As shown, the 21-element continuous-surface DM was able to fit the lowest 12 Zernike-mode aberrations pretty well, with fitting errors of less than 0.5.

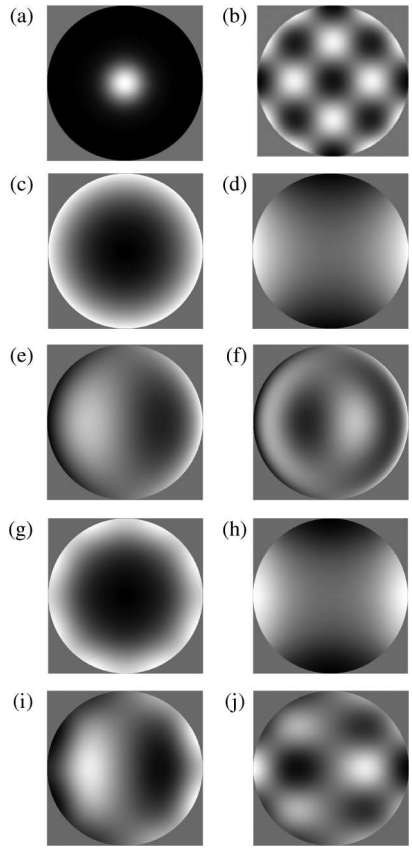

Fig. 8. Response function of the actuator and aberration fit of the 21-element DM. (a) Response function, (b) waffle mode, (c) $Z(2,0)$, (d) $Z(2,-2)$, (e) $Z(3,-1)$, (f) $Z(5,-1)$, and fitting results for (g) $Z(2,0)$, (h) $Z(2,-2)$, (i) $Z(3,-1)$, and (j) $Z(5,-1)$.

However, it was not able to fit the highest four Zernike-mode aberrations, which were mainly limited by the distributed spatial frequency of the DM actuators. The correction capability of the 21-element continuous-surface DM was not available for higher Zernike-mode aberrations. In the following experiment, the lowest 12 Zernike-mode aberrations were chosen as the correction objects for the HLAOS.

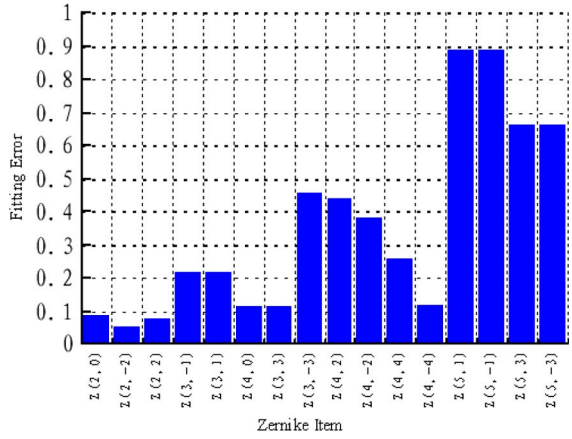

Fig. 9. Aberration fitting error of the 21-element DM.

5. HLAOS NUMERICAL SIMULATION

A schematic of the HLAOS is shown in Fig. 10, where the specific parameters of the HWFS are the same as in the aforementioned numerical simulation test, and the 21-element continuous-surface DM model is also similar to the one mentioned previously. BS1 and BS2 are two beam splitters. Twenty-four detection pinholes of 0.5 mm × 0.5 mm were selected at the center of each spot on the holographic image plane.

First, after loading incident light waves with aberrations into the experiment, the optical field distribution of the holographic image plane of the HWFS was solved. Then, the relative light intensity of each pair of spots was calculated using the light intensity data within the detection aperture to obtain the coefficients of each Zernike-mode aberration, thereby realizing Zernike-mode aberration decomposition of wavefront distortion. The wavefront controller performs proportional-integral-differential (PID) calculations for each Zernike-mode aberration, respectively, and then the numerical model of the 21-element continuous-surface DM is used to correct each Zernike-mode aberration. As incident light waves again, the corrected residual aberrations were made into iterative calculations to achieve a closed-loop correction.

As shown in Fig. 11(a), we loaded the RMS value of 0.63λ of the wavefront distortion in the experiment: $Z(2,0)$, $Z(2,-2)$, $Z(3,1)$, and $Z(3,3)$ are 0.3λ; $Z(4,0)$, $Z(4,-2)$, and $Z(4,-4)$ are 0.15λ. The laser spot on the focal plane of the system is shown in Fig. 11(b). The impact of the DM is first ignored and the DM is regarded as being able to correct aberrations detected by the wavefront sensor "ideally." When the adaptive optics system reached a steady state, the RMS value of the residual aberration was 0.034λ, as shown in Fig. 11(c), and the laser spot on the focal plane is shown in Fig. 11(d). After introducing the 21-element continuous-surface DM model and after the adaptive optics system reached a steady state, the RMS value of the residual aberration was 0.13λ, as shown in Fig. 11(e), and the laser spot on the focal plane is shown in Fig. 11(f).

To evaluate the dynamic correction ability of the adaptive optics system after the introduction of the 21-element continuous-surface DM model, the number of iterations was taken to be the abscissa coordinate and the RMS value of the residual aberration was the vertical coordinate, as shown in Fig. 12. The PID gain is 0.15. The red curve shows that the system could

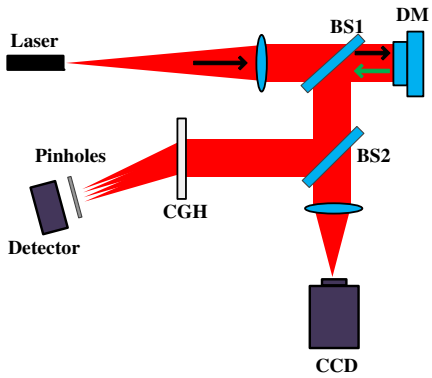

Fig. 10. Schematic of HLAOS.

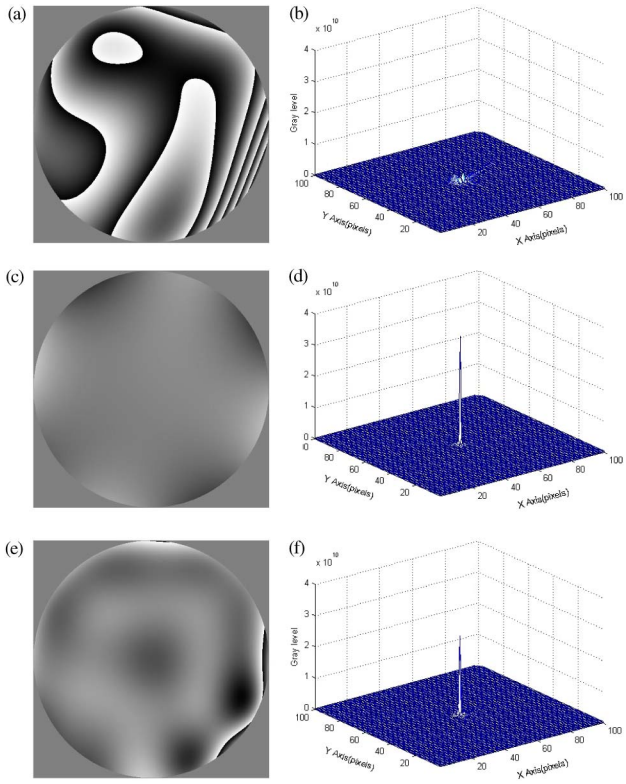

Fig. 11. (a) Loaded tested aberration, (b) system point spread function after loading aberration, (c) corrected wavefront of an "ideal" DM, (d) corrected point spread function of an "ideal" DM, (e) corrected wavefront of the 21-element DM, and (f) corrected point-spread function of the 21-element DM.

reach the steady state after approximately 15 iterations. The test results shown in Fig. 13 indicate a similar effect.

It should be noted that the initial RMS value of the wavefront aberration exceeded the maximum wavefront aberration coded into the HWFS. That is, the HLAOS cannot detect wavefront aberrations accurately for the first few corrections but the system can still reach the steady state because, even

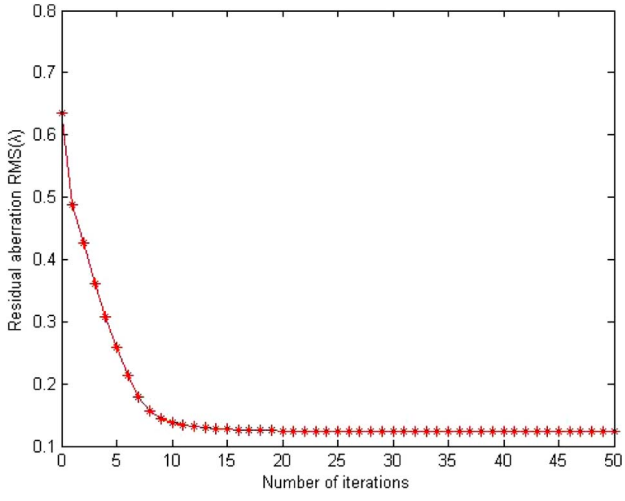

Fig. 12. Features of the dynamic response of HLAOS.

though the system cannot precisely detect the wavefront, it can detect the "trend" of each Zernike-mode aberration or "polarity." Therefore, the HLAOS can make each Zernike-mode aberration decrease gradually, ultimately minimizing the amplitude of each Zernike-mode aberration.

6. EXPERIMENT

We established the experimental setup shown in Fig. 14 to verify the simulation results. The output wavelength of the laser used in the experiment was 632.8 nm. The 21-element continuous mirror DM was used as a wavefront corrector, the working voltage of the piezoelectric transducer actuator was 0–110 V, and the pattern parameters of the actuators were the same as in the preceding numerical simulation experiments. The HWFS was composed of an SLM provided by BNS Corporation (256 × 256 pixels and 24 μm pixel pitch), a pinhole array, and an avalanche photodiode (APD) array in which the binary phase CGH was displayed by the SLM, as shown in Fig. 2. The SLM pupil diameter was 6 mm, the holographic image plane was 3000 mm away from the hologram (to reduce the system size, we folded the light path with a plane mirror), the holographic spot was more than 2 cm away from the axis, and the pinhole array aperture was 2 mm. The APD array was an SENSL SPM detector array, Array4p9, with a pixel number of 12 × 12 and pixel size of 3 mm. The dark count rate was 450 kHz. A self-made 37-unit Shack–Hartmann wavefront sensor was used to contrast the HWFS with a pupil diameter of 2.8 mm. BS1, BS2, and BS3 are three beam splitters. A beam expander was used to match the Shark–Hartmann wavefront sensor and HWFS pupil. The lens used for imaging had a focal length of 400 mm, which was used to assess the effect of the HLAOS wavefront correction. The imaging CCD pixel size was 4.65 μm and the frame rate was 6 frames/s.

Before the experiment, we set a non-common path aberration that was introduced by the beam expander at the minimum. Then, due to an alignment error in the pinhole array and an inhomogeneous error in the APD array, we needed to calibrate the HWFS's zero point. We made a beam of a standard reference plane wave enter the SLM and continuously recorded the response of the APD array 21 times, as shown in Fig. 15(a). Because the impact of noise arising from the APD can be observed clearly in the figure, the mean filtering method was adopted to improve the accuracy of the "zero point" calibration. Then, the Zernike aberration across various modes was given by the DM and the HWFS response sensitivity was calibrated by measuring the output signal of the APD array. The measured response sensitivity curves of $Z(2, 2)$ and $Z(3, 1)$ are shown in Figs. 15(b) and 15(c), respectively.

Comparing Figs. 4(b) and 15(c), the response curves measured in the experiment show that the HWFS responds to not only the aberration of $Z(3, 1)$ but also to those of $Z(2, 0)$ and $Z(3, -3)$ to some degree. This is because the nonlinear characteristics of the piezoelectric transducer actuator make it difficult for the DM to produce an ideal Zernike aberration. The DM loads not only the aberration of $Z(3, 1)$, but also those of $Z(2, 0)$, $Z(3, -3)$, etc. In other words, the crosstalk effect is not from the HWFS but from the DM. However, when building a

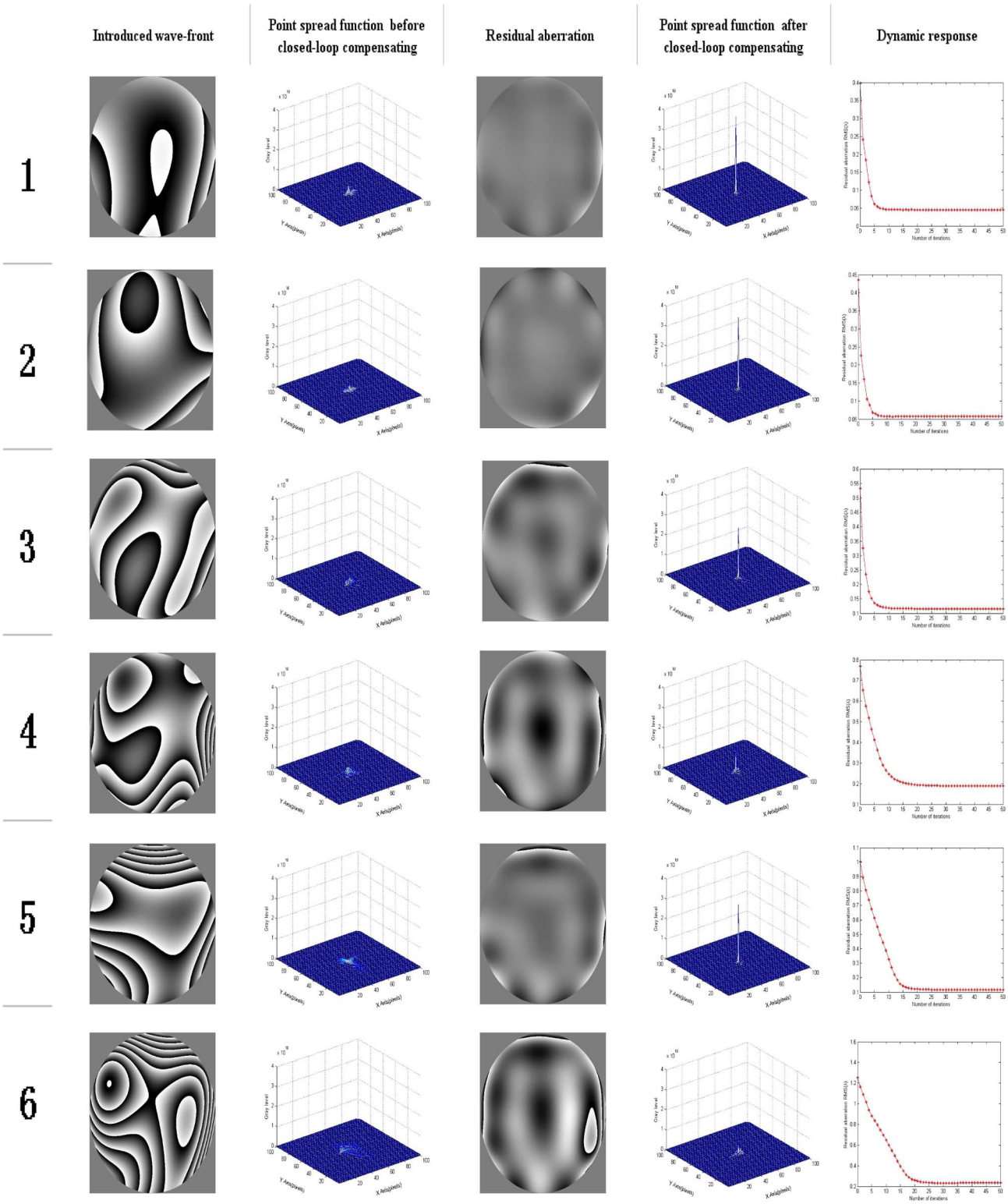

Fig. 13. Additional simulation results.

sensitivity matrix, we dealt with both of these in an indiscriminate way. In other words, a decoupling method based on the multiplex sensitivity matrix was applied.

After system calibration, we conducted a flattening experiment for the DM. When actuators of the 21-element continuous-surface DM were loaded with a voltage of 55 V, the imaging CCD collected the focal plane spot, as shown in Fig. 16(a). The focal plane light field distribution is shown in Fig. 16(b), where the Strehl ratio is 0.46. When the HLAOS worked in the closed-loop state and steadied, the imaging CCD

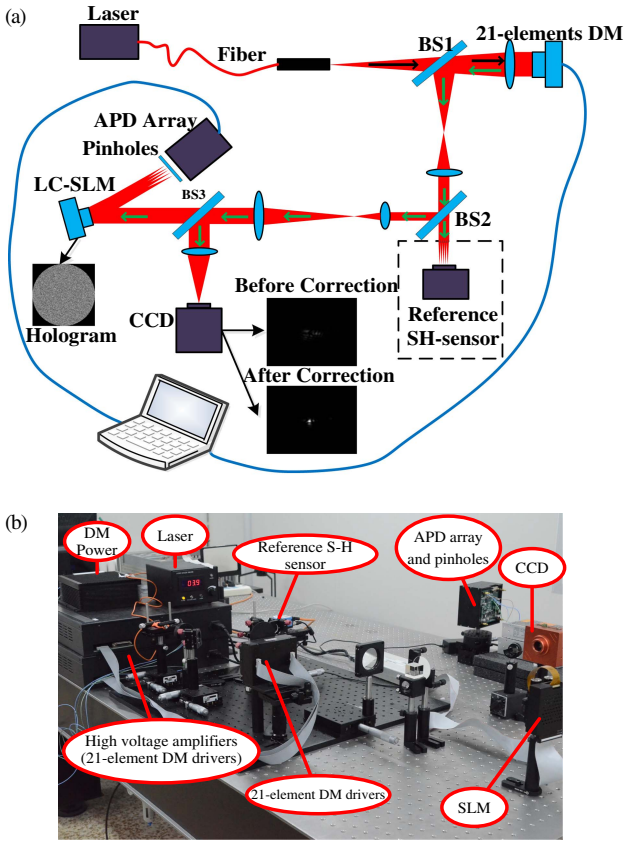

Fig. 14. (a) Schematic of the optical path and (b) image of the experimental setup.

collected the focal plane spot, as shown in Fig. 16(c), and the focal plane light field distribution, as shown in Fig. 16(d), where the Strehl Ratio is 0.80. We conducted a contrast experiment to assess the aberration-compensation effect of the HLAOS. To do this, we built a mature adaptive optics system with a 37-unit Shack–Hartmann wavefront sensor and a 21-element continuous-surface DM. After it compensates for the aberration, the imaging CCD collected the focal plane spot, as shown in Fig. 16(e), and the focal plane light field distribution, as shown in Fig. 16(f), where the Strehl Ratio is 0.82. Figure 17 shows the focal plane spot after the 1st, 2nd, 3rd, and 10th corrections using the HLAOS. We evaluated the HLAOS dynamic response with the Strehl Ratio of the focal plane spot of the imaging camera, as shown in Fig. 18.

Although the final wavefront-correction effect was slightly poorer than that of a traditional adaptive optics system based on the 37-unit Shark–Hartmann wavefront sensor, the use of an APD array detector with lower noise will achieve a more accurate zero-point calibration and better correction effect. In addition, the aberrations of tilt and tip were not detected in the experiment. Instead, the optical adjustment was made and a pinhole array with a larger aperture was selected to avoid its influence. The location of the zeroth-order diffracted light spot can be used in future engineering systems to detect the tilt and tip, and the DM can be used for correction, which will help improve the aberration-compensation effect.

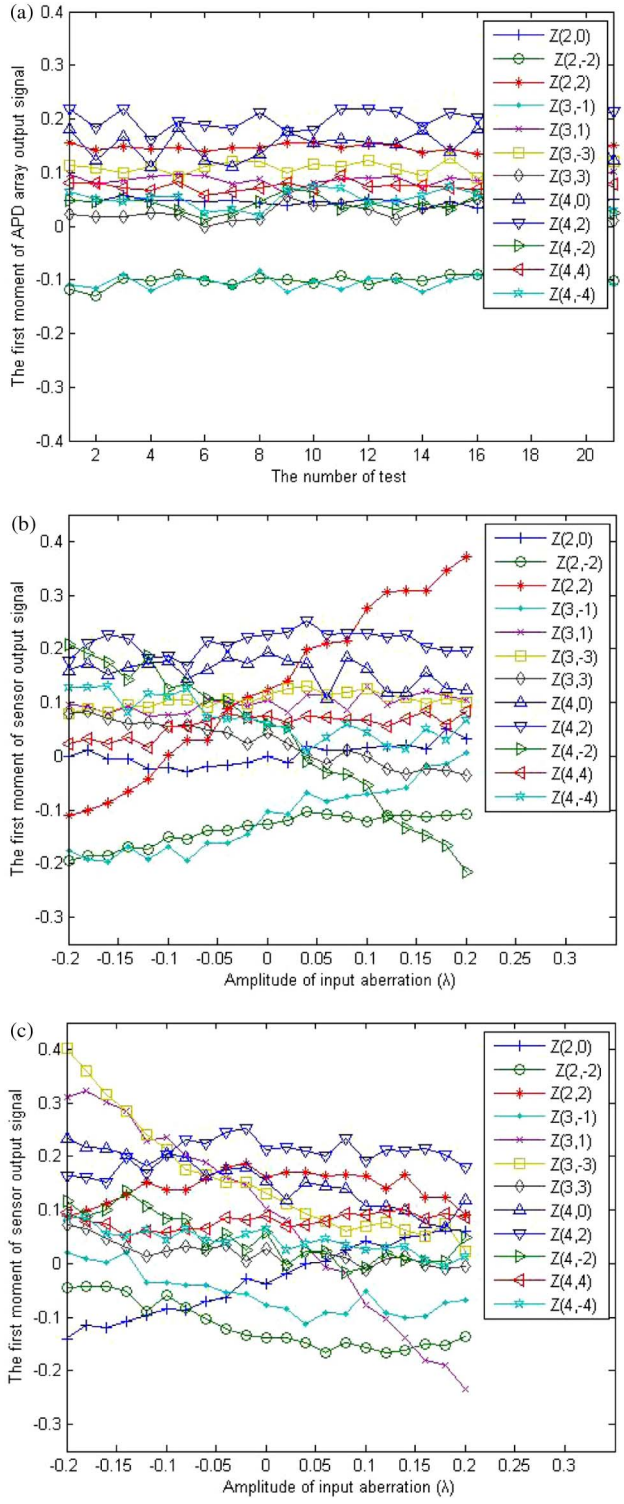

Fig. 15. Zeros and sensitivity response curve of the HWFS. (a) Zeros of the HWFS and sensitivity response curves of (b) $Z(2,2)$ and (c) $Z(3,1)$.

7. CONCLUSION

A HWFS and 21-element continuous-surface piezoelectric DM were used to establish a HLAOS. The aberration-detection method of the HWFS was theoretically elaborated, and a

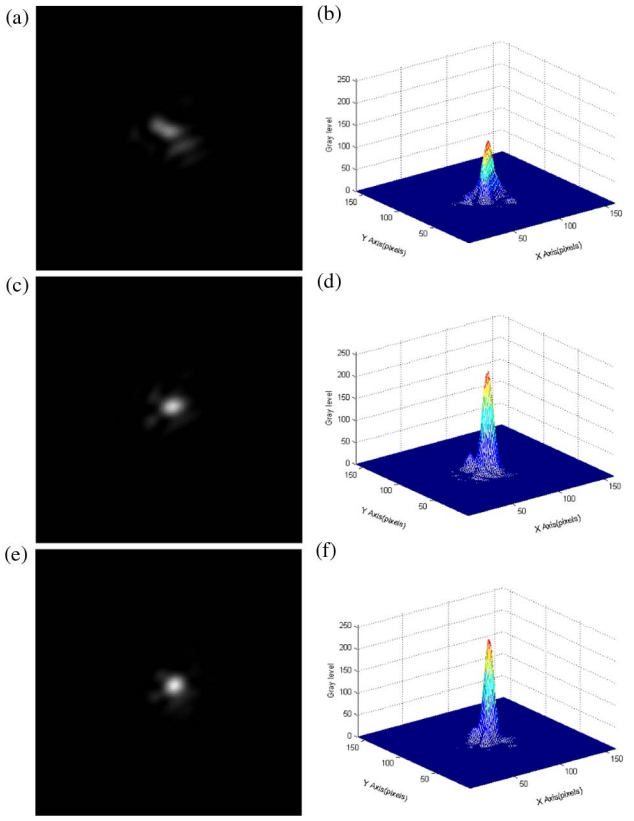

Fig. 16. (a) and (b) power distributions on the focus plane before compensating for aberrations. Power distributions on the focus plane after compensating for aberrations using [(c) and (d)] the HLAOS and [(e) and (f)] the SHLAOS.

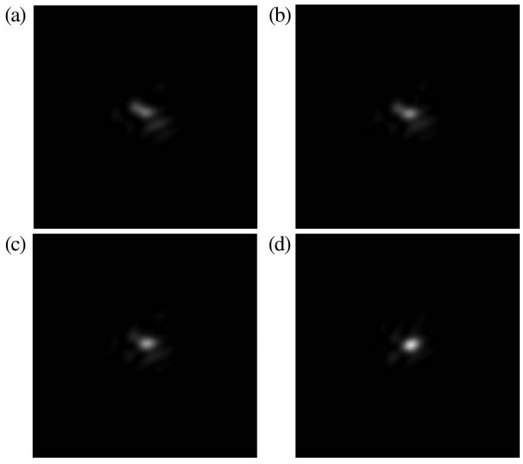

Fig. 17. Focal plane spot collected by imaging CCD after the (a) 1st, (b) 2nd, (c) 3rd, and (d) 10th corrections using the HLAOS.

numerical model of the 21-element continuous-surface DM was established. Based on this model, the fitting ability of the 21-element continuous-surface DM to Zernike-mode aberrations was analyzed and the closed-loop correction process of the HWFS was simulated numerically to the lowest 12 Zernike-mode aberrations. The simulation results showed that

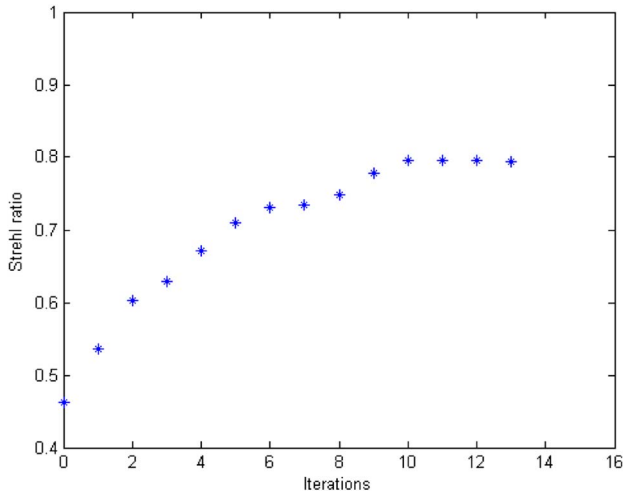

Fig. 18. Improvement of the Strehl ratio as a function of iterations.

effective correction of a distorted wavefront can be achieved by a HLAOS via several closed-loop corrections, and the wavefront-fitting ability of the 21-element continuous-surface piezoelectric DM was the main factor affecting the wavefront-correction accuracy of the HLAOS. The experimental setup was established and the result showed that a HLAOS can achieve a comparable aberration-compensation effect to that of a traditional adaptive optics system.

Funding. National Natural Science Foundation of China (NSFC) (61605199, 61601195).

Acknowledgment. The authors acknowledge helpful suggestions from the reviewers and help from the editors.

REFERENCES

1. M. A. van Dam, A. H. Bouchez, D. Le Mignant, and P. L. Wizinowich, "Quasi-static aberrations induced by laser guide stars in adaptive optics," Opt. Express **14**, 7535–7540 (2006).
2. Z. Renzhong, *Adaptive Optics* (National Defence Industry, 1996).
3. M. A. A. Neil, M. J. Booth, and T. Wilson, "New modal wavefront sensor: a theoretical analysis," J. Opt. Soc. Am. A **17**, 1098–1107 (2000).
4. M. A. A. Neil, M. J. Booth, and T. Wilson, "Closed-loop aberration correction by use of a modal Zernike wavefront sensor," Opt. Lett. **25**, 1083–1085 (2000).
5. A. Zepp, "Analogue holographic wavefront sensor: a performance analysis," Proc. SPIE **9614**, 96140G (2015).
6. F. Ghebremichael, G. P. Andersen, and K. S. Gurley, "Holography-based wavefront sensing," Appl. Opt. **47**, A62–A69 (2008).
7. G. P. Andersen, L. Dussan, F. Ghebremichael, and K. Chen, "Holographic wavefront sensor," Opt. Eng. **48**, 085801 (2009).
8. G. P. Andersen, F. Ghebremichael, and K. S. Gurley, "Fast computing-free wavefront sensing," in *Adaptive Optics: Analysis and Methods/Computational Optical Sensing and Imaging/Information Photonics/Signal Recovery and Synthesis Topical Meetings on CD-ROM*, OSA Technical Digest (CD) (Optical Society of America, 2007), paper AWC4.
9. S. K. Mishra, R. Bhatt, D. Mohan, A. K. Gupta, and A. Sharma, "Differential modal Zernike wavefront sensor employing a computer-generated hologram: a proposal," Appl. Opt. **48**, 6458–6465 (2009).
10. R. Bhatt, S. K. Mishra, D. Mohan, and A. K. Gupta, "Direct amplitude detection of Zernike modes by computer-generated holographic

wavefront sensor: modeling and simulation," Opt. Lasers Eng. **46**, 428–439 (2008).
11. G. Andersen, P. G. Austin, R. Gaddipati, P. Gaddipati, and F. Ghebremichael, "Fast, compact, autonomous holographic adaptive optics," Opt. Express **22**, 9432–9441 (2014).
12. F. Kong and A. Lambert, "Improvements to the modal holographic wavefront sensor," Appl. Opt. **55**, 3615–3625 (2016).
13. P. M. Palomo, A. Zepp, and S. Gładysz, "Characterization of the digital holographic wavefront sensor," Proc. SPIE **9242**, 92421T (2014).
14. E. Anzuola, A. Zepp, P. M. Palomo, S. Gladysz, and K. Stein, "Holographic wavefront sensing for atmospheric turbulence using Karhunen–Loève decomposition," in *Imaging and Applied Optics*, OSA Technical Digest (online) (Optical Society of America, 2016), paper AOM4C.2.
15. L. Changhai and J. Zongfu, "Holographic modal wavefront sensor: theoretical analysis and simulation," Chin. J. Lasers **36**, 147–152 (2009).
16. L. Changhai, X. Fengjie, M. Haotong, H. Shengyang, and J. Zongfu, "Modal wavefront sensor based on binary phase-only multiplexed computer-generated hologram," Appl. Opt. **49**, 5117–5124 (2010).
17. L. Changhai, X. Fengjie, H. Shengyang, and J. Zongfu, "Performance analysis of multiplexed phase computer-generated hologram for modal wavefront sensing," Appl. Opt. **50**, 1631–1639 (2011).
18. A. D. Corbett, T. D. Wilkinson, J. J. Zhong, and L. Diaz-Santana, "Designing a holographic modal wavefront sensor for the detection of static ocular aberrations," J. Opt. Soc. Am. A **24**, 1266–1275 (2007).
19. S. Dong, T. Haist, W. Osten, T. Ruppel, and O. Sawodny, "Response analysis of holography-based modal wavefront sensor," Appl. Opt. **51**, 1318–1327 (2012).
20. S. Dong, T. Haist, and W. Osten, "Hybrid wavefront sensor for the fast detection of wavefront disturbances," Appl. Opt. **51**, 6268–6274 (2012).
21. K. Yao, J. Wang, X. Liu, and W. Liu, "Closed-loop adaptive optics system with a single liquid crystal spatial light modulator," Opt. Express **22**, 17216–17226 (2014).
22. W. Liu, W. Shi, K. Yao, and P. Wu, "Fiber coupling efficiency analysis of free space optical communication systems with holographic modal wave-front sensor," Opt. Laser Technol. **60**, 116–123 (2014).
23. X. D. Lin, X. Y. Liu, J. L. Wang, P. F. Wei, and F. G. Wang, "Study on the flatten calibration of the deformable mirror based on the measurement of the interferometer," Acta Photon. Sin. **41**, 511–515 (2012).